Tryptophan Rotamers as Evidenced by X-Ray, Fluorescence Lifetimes, and Molecular Dynamics Modeling

Samuel L. C. Moors,* Mario Hellings,† Marc De Maeyer,‡ Yves Engelborghs,† and Arnout Ceulemans*
*Laboratory of Quantum Chemistry, †Laboratory for Bio-Molecular Dynamics, and ‡Laboratory for Bio-Molecular Modeling, University of Leuven, Leuven, Belgium

ABSTRACT We investigated the native-state dynamics of the *Bacillus caldolyticus* cold-shock protein mutant *Bc*-Csp L66E, using fluorescence and appropriate molecular dynamics methods. Two fluorescence lifetimes were found, the amplitudes of which agree very well with tryptophan rotamer populations, obtained from parallel tempering calculations. Rotamer lifetimes were predicted by transition-state theory from high-temperature simulations. Transition pathways were extracted from the transition rates between individual rotameric states. The molecular dynamics also reveal the loop fluctuations in the native state.

INTRODUCTION

Side-chain rotamers located at the protein surface play a key role in various biological processes, including protein-ligand binding (1), protein-protein recognition (2), protein-DNA binding (3), protein folding (4,5), and stability (6). If we want to fully understand (and ultimately predict) all those processes, we need to know the different rotamer populations, their stability, and the important factors that contribute to their equilibrium distribution.

Rotamers may also be used as probes for protein dynamics. Tryptophan fluorescence spectra, quantum yields, and lifetimes depend highly on the surrounding electric field (7–10). The main fluorescence quenching mechanism is believed to be electron transfer (11). Relating tryptophan fluorescence lifetimes to the local environment is complicated by the multi-exponential decay observed in most proteins. In recent years, much experimental and theoretical work has been published that suggests the existence of rotameric states as the source of this multi-exponential decay (12–17). Other proposed mechanisms include reversible electron transfer of the excited tryptophan (18), spectral relaxation of the excited state (19), and energy transfer to different acceptors (20). Until now, no exclusive evidence has been given for the rotamer model or for any other model.

Here, we investigate the basic conditions for the rotamer model using computational methods. If rotamers are the cause of multiple fluorescence lifetimes, these rotamers should be sufficiently populated and have rotamer lifetimes exceeding the corresponding fluorescence lifetimes. As a first indication for the existence of rotamers, we considered a small protein of which the x-ray structure suggests two equally populated Trp conformations: the *Bacillus caldolyticus* cold-shock protein mutant *Bc*-Csp L66E with Protein Data Bank (PDB) code 1HZB (21).

Cold-shock proteins (CSPs) represent a widespread family of small proteins that contain the conserved nucleic-acid-binding cold-shock domain (CSD). The CSD harbors the nucleic-acid-binding motifs RNP-1 and RNP-2. Many CSPs are expressed after a cold shock (22). *Bc*-Csp is a 66-residue β-barrel consisting of five antiparallel β-strands. This thermostable protein has been extensively studied for its folding kinetics and its stability in relation to its homolog *Bs*-CspB from the mesophylic *Bacillus subtilis* (23–26). The x-ray structure of 1HZB resembles strongly the conformation of its wild-type counterpart (PDB code 1C9O). The stability of 1HZB is situated between *Bs*-CspB and *Bc*-Csp.

To study these dynamical aspects, parallel tempering (PT), or replica-exchange molecular dynamics, allow us to obtain a statistical distribution of the protein conformational space in a very efficient and rigorous way (27,28). The method has been used for studying folding of proteins containing up to 46 residues in explicit solvent (29). For larger proteins, however, simulation times become prohibitively long. By limiting the search space to the native state and by including volume exchanges as well as temperature exchanges, we were able to explore the local dynamics in great detail.

MATERIALS AND METHODS

Materials

Bc-Csp was purified as described by Mueller et al. (30) and donated by Prof. Dr. F. X. Schmid. Acrylamide and *N*-acetyltryptophanamide were purchased from Sigma Chemical (St. Louis, MO). All other chemicals were analytical grade. Distilled and deionized water (ddH_2O) was used throughout the experiments. The buffer solution used for the fluorescence measurements contained 25 mM Tris, pH 8.2, 2.5 mM $CaCl_2$, and 50 mM NaCl. All solutions were filtered through a 0.22-μm filter (Millipore, Bedford, MA) and were spectroscopically pure.

Time-resolved fluorescence decay

Fluorescence lifetimes were measured using automatic multi-frequency phase fluorometry between 1.6 MHz and 1 GHz as described previously

Submitted March 15, 2006, and accepted for publication April 25, 2006.

Address reprint requests to Arnout Ceulemans, Laboratory of Quantum Chemistry, University of Leuven, Celestijnenlaan 200F, B-3001 Leuven, Belgium. Tel.: 32-1632-7363; Fax: 32-1632-7992; E-mail: Arnout.Ceulemans@chem.kuleuven.be.

0006-3495/06/08/816/08 $2.00

doi: 10.1529/biophysj.106.085100

(12). *N*-acetyltryptophanamide in ddH_2O with a fluorescence lifetime of 3.059 ns (at 22°C) was used as reference. Data analysis was performed using a nonlinear least-squares algorithm (31). Measurements performed at different emission wavelengths (330–380 nm, 10-nm intervals) were analyzed simultaneously with global analysis (Globals Unlimited) to improve the recovery of lifetimes and amplitude fractions (32). The data were fitted using the modified Levenberg-Marquardt algorithm, assuming that the fluorescence lifetimes are independent of the wavelength (33). Quantum yields, radiative rate constant, and wavelength-independent amplitude fractions were determined as described by Hellings et al. (17).

Fluorescence quenching

The quenching of Trp^8 in *Bc*-Csp wild-type (10 μM) with increasing amounts of quencher was performed by adding aliquots of a freshly prepared 1-M acrylamide stock solution to the cuvette, after which the changes in the fluorescence lifetimes τ_i and corresponding amplitude fractions α_i were monitored. The dependency of the reciprocal fluorescence lifetime on the quencher concentration was fitted by the classical Stern-Volmer equation (34) and used to calculate the quenching constant k_q.

Dead-end elimination method

The dead-end elimination (DEE) method (35) was used to determine the possible Trp conformations in *Bc*-Csp 1HZB. Briefly, the method uses an extensive rotamer library and combines possible rotamers to find the global minimum energy conformation (GMEC) for a given backbone structure. A smart elimination of rotamers that cannot be part of the GMEC avoids the combinatorial explosion and makes the calculation of the GMEC possible. The identification of the rotamer clusters occurred as previously described by Hellings et al. (17). A full-hydrogen model and energy-minimized x-ray structure (PDB code 1HZB) was used as the starting structure. The used rotamer library was an enhanced version of the library of De Maeyer et al. (36). The DEE algorithm has been implemented in the BRUGEL package (37) using the CHARMM force field (38).

Molecular-dynamics simulations

All molecular-dynamics (MD) simulations were performed using the Amber 2003 force field (39) with a modified version of the Amber 8 software (40). The smooth Particle-mesh Ewald method (41) was employed to accommodate long-range electrostatic forces. The nonbonded cut-off for van der Waals interactions was set to 9 Å. Covalent bonds involving hydrogen atoms were constrained using SHAKE (42). A time step of 1 fs was used. Samples were collected every 0.1 ps. The temperature was controlled using the weak-coupling algorithm (43). The initial structure was obtained from monomer A of the x-ray structure of *Bc*-Csp 1HZB (Trp^8 $\chi1 = 70°$, $\chi2 = -97°$). Three sodium ions were added in a shell around the protein using a Coulombic potential on a grid. The neutralized protein was solvated in a truncated octahedral box containing 3190 TIP3P (44) water molecules. Minimization was carried out in three stages. First, the solvent was relaxed for 10,000 steps, keeping the solute restrained. Next, the protein was relaxed for 10,000 steps with restraints on the solvent. In the third stage, both solute and solvent were relaxed for 15,000 steps with no restraints. The backbone root mean-square deviation (bRMSD) between the relaxed protein and the x-ray structure was 0.62 Å. To improve sampling of the native state, the protein was allowed to move freely below 2.5 Å bRMSD from the relaxed x-ray structure. Above this threshold, the system was penalized by a harmonic restraint on the bRMSD with a force constant of 10 kcal mol^{-1} $Å^{-2}$. Solvent-accessible surface areas (SASA) were calculated using the program NACCESS (45), which is an implementation of the Lee and Richards method (46). Secondary structures were assigned with the program DSSPcont (47), which is a continuous version of the discrete classification used by the DSSP (48) program. Contacts are defined as occurring whenever the C_α atoms of two nonneighboring amino acids are within 6.5 Å of each other. The fraction of native contacts (Q) is taken as the fraction of contacts found in the relaxed x-ray structure, which contains 134 contacts.

Parallel tempering

The PT simulation was carried out based on the method of Paschek and García (49). Trial swaps were performed between replicas with different temperatures and volumes. The acceptance probability for replica exchange between two states i and j with corresponding temperatures T_i and T_j and box volumes V_i and V_j is given by

$$P_{\mathrm{acc}} = \min\{1, \exp[\beta_i(U(x_i)^{V_i} - U(x_j)^{V_i}) - \beta_j(U(x_i)^{V_j} - U(x_j)^{V_j})]\}, \quad (1)$$

with $\beta = 1/kT$ and $U(x)^V$ being the potential energy of the state with coordinates x and volume V. The energy $U(x_i)^{Vj}$ is approximated as

$$U(x_i)^{V_j} \approx U(x_i)^{V_i} - (P'_i - M/\beta'_i V_i) \times (V_j - V_i), \quad (2)$$

where M represents the number of molecules in the simulation box. P'_i and β'_i denote the instantaneous pressure and temperature. An analogous expression is used for $U(x_j)^{Vi}$.

It was observed that, for efficient sampling of the Trp^8 $\chi2$ dihedral angle space, decreased densities and high temperatures were necessary since when the system was heated without decreasing the density, $\chi2$ transitions became very unlikely due to the high system pressure. Therefore, 32 replicas were distributed exponentially over a 300–645 K temperature range and evenly over a 1.02–0.65 g cm^{-3} density range. Temperature and volume exchange moves occurred simultaneously. Volume changes were performed such that only intermolecular distances were altered. It is important to note that sudden volume changes can cause considerable nonequilibrium effects, even if those volume changes are small. This was evidenced by jumps in the potential energy plots (data not shown). To alleviate this behavior, densities were allowed to change gradually over a time period of 0.25 ps, followed by a 0.25-ps equilibration time before data collection.

For the generation of starting conformations, each replica was heated to its target temperature, changed gradually to its desired density, and subsequently simulated for 0.5 ns without replica-exchange moves. Replicas were simulated in the *NVT* ensemble. The time constant for temperature coupling was 0.5 ps. Exchanges were attempted every 0.5 ps. Acceptance probabilities varied between 0.08 and 0.20. The PT simulation was carried out for 16.2 ns per replica, from which the last 11.8 ns were used to calculate the reported thermodynamic properties. Standard errors of the thermodynamic averages were calculated using the statistical inefficiency method (50).

High-temperature MD

Constant pressure simulations (1 bar) were carried out for eight runs at five different temperatures: 425 K, 450 K, 475 K, 500 K, and 525 K. Starting coordinates and velocities were collected form 1-ns simulations at temperatures ranging between 500 K and 600 K. The structures were equilibrated for another nanosecond. The first transition of every run was discarded. Simulation times ranged between 12 ns for the highest- and 22.8 ns for the lowest-temperature run, with an aggregate simulation time of 560 ns.

The total transition rate constant $k_{tot,i}$ (T), defined as the sum of all rate constants $k_{j,i}$ (T) originating from rotamer i at temperature T ($k_{tot,i}(T) = \sum_j k_{j,i}(T)$), was calculated by numerical integration (51)

$$k_{tot,i}(T) = 1/\int_0^\infty f(t_i)dt, \quad (3)$$

where $f(t_i)$ is the fraction of residence times longer than t_i within the boundaries of rotamer i. The boundary of a rotamer was taken as the contour line in $\chi1 \times \chi2$ space that contains 95% of its population (see Fig. 5). When

the side-chain torsion angles were outside any rotamer boundary, it was assigned as its last visited rotamer state. Using the high-temperature rate constants, we extrapolated kinetic data at room temperature from transition state theory by construction of Eyring plots (see Fig. 4). Individual rate constants $k_{j,i}$ from rotamer i to j were computed as

$$k_{j,i}(T) = k_{tot,i}(T) \times N_{j,i}(T)/N_{tot,i}(T), \quad (4)$$

where $N_{j,i}$ is the number of transitions from i to j and $N_{tot,i}$ is the total number of transitions originating form i. From the individual transition rate constants, the relative equilibrium concentrations C_i were computed by solving the set of six homogeneous linear equations

$$dC_i/dt = \sum_{j\neq i} k_{i,j}(T)C_j - \sum_{j\neq i} k_{j,i}(T)C_i = 0. \quad (5)$$

Rotamer transition pathways were determined on the basis of mean first passage times (MFPT) for discrete kinetics (52). The MFPT τ_{bi} from state i to b is given by

$$\begin{aligned} &\tau_{bi} = \sum_j K_{ji}^{-1}, \quad K_{ji} = k_{ji} \quad \text{for } i \neq j \quad \text{and} \quad i,j \neq b \\ &K_{ii} = -\sum_{j\neq i} k_{ji} \quad \text{for } i \neq b \\ &K_{ib} = K_{bi} = 0, \end{aligned} \quad (6)$$

where K_{ji}^{-1} is the inverse matrix of the matrix K_{ji} and k_{ji} is the individual transition rate from rotamer i to j. The transition path from rotamer state a to b is defined as the path for which each intermediate step from state i to j maximizes $g_{ji}^{b} = k_{ji}(\tau_{bi} - \tau_{bj})$. For the first step, $i = a$, and for the last step, $j = b$.

Nomenclature

Rotamer nomenclature was taken from Lovell et al. (53). Thus, for Trp $\chi 1$, we used **t**, **m,** and **p**, representing *trans*, minus 60°, and plus 60°, respectively. Trp $\chi 2$ values were rounded to the nearest 5°.

RESULTS AND DISCUSSION

Fluorescence lifetimes

The fluorescence decay of Trp^8 in *Bc*-Csp was measured at emission wavelengths ranging from 330 to 380 nm in 10-nm intervals. The decay curves were analyzed by single-curve analysis of the data at each wavelength and global analysis of data for seven emission wavelengths. The lowest χ^2 value, defined as the correctness of fit, was obtained with a double exponential fit, yielding lifetime components $\tau_1 = 2.45$ ns and $\tau_2 = 6.16$ ns with respective amplitude fractions $\alpha_1 = 0.29$ and $\alpha_2 = 0.71$ (Table 1).

Fluorescence quenching with acrylamide

To investigate the solvent accessibility of the two lifetime components, an acrylamide quenching study was performed. The measurements were done at 350 nm. The results are shown in Table 1. Both reciprocal lifetimes show a linear dependency on the acrylamide concentration. The bimolecular quenching constants k_{q1} and k_{q2} are 2.63 ± 0.12 M^{-1} ns^{-1} and 1.80 ± 0.09 M^{-1} ns^{-1} for τ_1 and τ_2, respectively, indicating that the shortest lifetime components correspond to the most solvent accessible rotameric state.

Native-state dynamics

We used the parallel tempering scheme for studying the dynamics of the folded protein. To improve sampling of the native state, the protein was allowed to move freely below 2.5 Å bRMSD from the relaxed x-ray structure. Above this threshold, the system was penalized by a harmonic restraint on the bRMSD. This approximation is valid if three conditions are met. First, the native state should be the dominant state at room temperature (this is true for most proteins). Second, rotamer transitions in the native state must occur on timescales much smaller than folding-unfolding transitions, indicating that the rotamer transition does not require unfolded conformations. Third, the native-state basin should be within the imposed threshold of 2.5 Å around the relaxed x-ray structure. For 1HZB, which folds in a two-state N ↔ U reaction, the first condition has been experimentally confirmed, with native- and unfolded-state lifetimes $\tau_N = 350$ ms and $\tau_U = 1.5$ ms (54). The second condition is satisfied for Trp^8, as will be shown below. For the third condition, we do not know the space occupied by the native state beforehand. However, recent theoretical and experimental studies suggest that protein-folding funnels are very narrow, with estimated maximum backbone variation ranging between 1 Å and 2 Å (55–58).

Fig. 1 *a* represents the free energy as a function of bRMSD and the fraction of native contacts (Q). Within the confined space of 2.5 Å, the native state bRMSD ranges over 1.5 Å. Two free-energy wells, with minima at 1.7 Å and 2.35 Å bRMSD, are connected by a small low-energy pathway and have relative populations of 0.69 and 0.31, respectively. The observed bRMSD values from the relaxed x-ray structure are

TABLE 1 Trp^8 fluorescence lifetimes and amplitude fractions in *Bc*-Csp

α_1	τ_1 (ns)	α_2	τ_2 (ns)	χ^{2*}	Acrylamide† (M)
0.29 ± 0.06	2.45 ± 0.03	0.71 ± 0.06	6.16 ± 0.14	1.36	0.00
0.27 ± 0.04	1.86 ± 0.05	0.73 ± 0.05	3.94 ± 0.10	1.22	0.05
0.28 ± 0.06	1.52 ± 0.09	0.72 ± 0.07	2.96 ± 0.12	1.30	0.10
0.25 ± 0.09	1.12 ± 0.10	0.75 ± 0.08	1.85 ± 0.09	1.59	0.20
0.27 ± 0.08	0.84 ± 0.11	0.73 ± 0.07	1.39 ± 0.15	1.61	0.30
0.26 ± 0.05	0.65 ± 0.08	0.74 ± 0.05	1.15 ± 0.11	1.45	0.40

*The value that defines the correctness of the fit.
†Quenching of Trp^8 in *Bc*-Csp (10 μM) with increasing amounts of acrylamide.

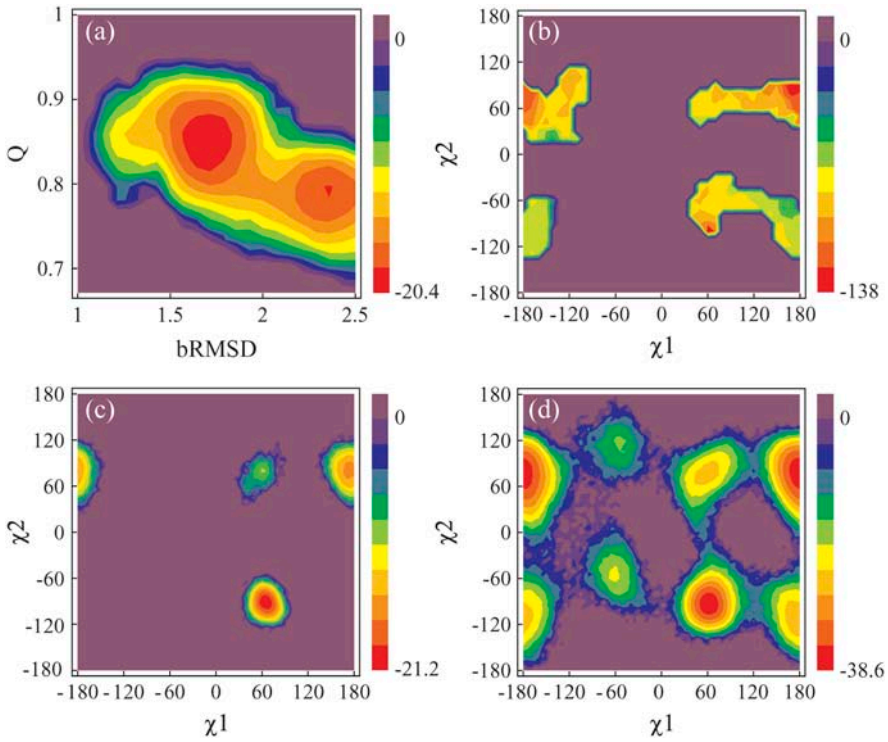

FIGURE 1 Energy contour maps in units of kJ mol^{-1}. (*a*) Free energy as a function of Q and bRMSD, from PT. The highest bRMSD well corresponds with a loss of the 3_{10}-helix structure. (*b*) Potential energy in function of Trp^8 $\chi1$ and $\chi2$, from DEE. The energies are calculated as the total nonbonded energies E_{totnb} for all structures with a negative E_{totnb}. Free energy in function of Trp^8 $\chi1$ and $\chi2$ from (*c*) PT and (*d*) 500 K MD. The relative free energy ΔG between two states i and j with relative populations P_i and P_j is calculated as $\Delta G = G_j - G_i = -RT\ln(P_j/P_i)$, where R denotes the universal gas constant.

attributed mainly to the loops, as the β-sheet bRMSD stays below 1 Å and is nearly independent of the total bRMSD (data not shown). The loop fluctuations are also evident from Figs. 2 and 3 *a*, and agree well with ^{15}N relaxation data on *Bs*-CspB (59). As expected, the largest fluctuations are found in the longest loop connecting the sheets $\beta3$ and $\beta4$. Also, loop $\beta4$-$\beta5$ experiences considerable fluctuation. The total RMS fluctuation of Arg^{56} on the loop between $\beta4$-$\beta5$ is remarkably high (Figs. 2 *b* and 3 *a*), with the guanidine group reaching out far from the protein core or making close contact with the CSD ($\beta2$ and $\beta3$). Keeping in mind the strong arginine-nucleic acid binding potential, we suggest that Arg^{56} acts as an antenna for possible nearby nucleic acid strands, and subsequently brings them into contact with the nucleic acid binding domain.

A high flexibility does not imply a total lack of structure. In particular, the 3_{10}-helix (Phe^{30}-Thr^{31}-Ala^{32}), which is present in all CSP crystal structures but absent in all NMR solution structures in the PDB to date, makes up a vital part of the molecule and is extrastabilized by a β-bridge between Ile^{33} and Val^{63} (Figs. 2, *orange*, and 3, *b* and *c*). Both structural elements are especially well preserved in the lower, but largely destroyed in the higher, free-energy well (Fig. 3, *b* and *c*).

Tryptophan rotamers

The 1HZB crystal structure (21) is dimeric, though *Bc*-Csp and mutants have been shown to exist as monomers in solution (60). Trp^8 of monomer B is disordered, containing two distinct conformations with equal occupancies (**p**−95° and **t**100°), whereas the Trp^8 side chain of monomer A occupies only **p**−95°.

Applying the DEE method, as defined by Hellings et al. (17), on Trp^8 of *Bc*-Csp 1HZB identified two rotamer clusters (Fig. 1 *b*) with energy minima at **p**−100° and **t**90°. These two clusters correspond to the two x-ray Trp conformations. However, the energy plot reveals also clusters for the rotamer **p**70°, as can be expected for a solvent-exposed residue. The PT calculation produced matching rotamers **p**−90° and **t**80° (Fig. 1 *c*), with respective populations 0.71 and 0.27 (Table 2). These values agree remarkably well with the amplitude fractions α_2 (0.71) and α_1 (0.29) of the fluorescence lifetimes τ_2 and τ_1 (Table 1). Furthermore, if we assign **p**−90° to τ_1 and **t**80° to τ_2, fluorescence quenching constants k_{q1} and k_{q2} correlate with average solvent accessibilities (Tables 1 and 2). Comparison with DEE demonstrates the importance of explicit solvent and/or backbone dynamics on the rotamer distribution, despite the small local backbone fluctuation. Nevertheless, DEE was able to identify the two most stable PT rotamers, which demonstrates the usefulness of this computationally inexpensive method as a rough estimation of rotamers.

Side-chain kinetics

For the three rotamers observed with PT, we applied transition-state theory to the high-temperature MD simulations to obtain total transition rate constants at room temperature. The

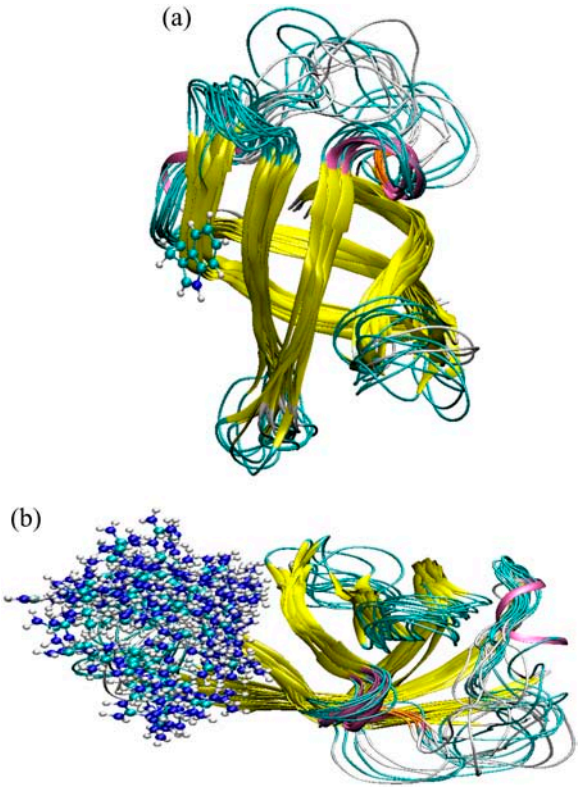

FIGURE 2 Superposition of 15 native-state structures of 1HZB from PT. The structures were carefully chosen to represent the occupied conformational space. The color scheme is as follows: 3_{10}-helix (*mauve*), extended β-strand (*yellow*), isolated β-bridge (*orange*), hydrogen-bonded turn (*cyan*), and coil (*white*). To these ribbon models were added in ball-and-stick models the side chains of (*a*) Trp^{8} in the $\mathbf{p}-90°$ state, and (*b*) 118 Arg^{56} conformations.

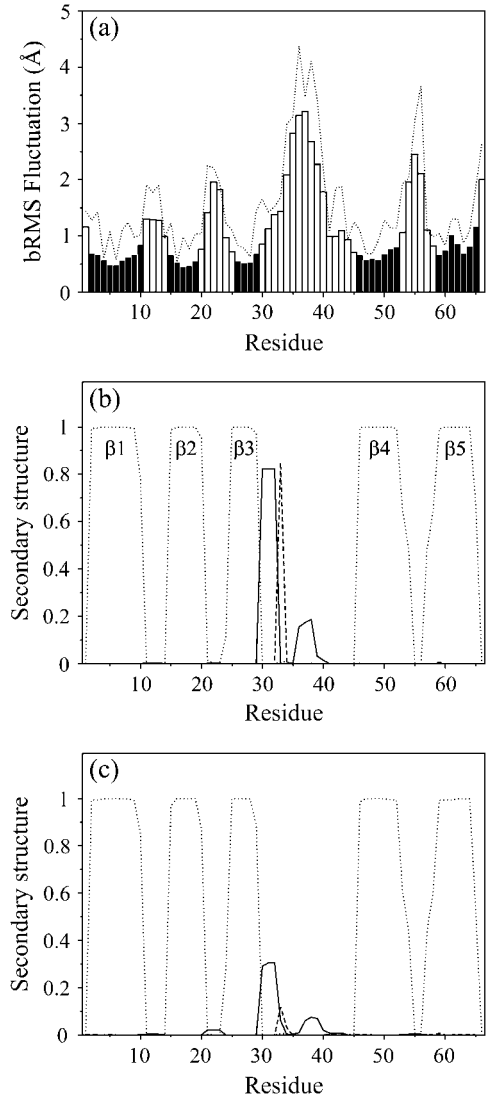

FIGURE 3 (*a*) bRMS fluctuation (*bars*) and total RMS fluctuation (*dotted line*) as a function of the residue number, from PT. The black bars indicate β-sheet residues. (*b* and *c*) Secondary-structure content in function of residue number for states belonging to (*b*) the low-bRMSD free-energy well and (*c*) the high-bRMSD free-energy well (see Fig. 1 *a*). Curves represent the 3_{10}-helix (*solid lines*), isolated β-bridge (*dashed lines*), and extended β-strand (*dotted lines*).

Eyring plots (Fig. 4) tell us that $\mathbf{p}-90°$ is the most kinetically stable rotamer below 475 K, whereas above 475 K $\mathbf{t}80°$ has a higher free energy of activation. This is due to both a higher $\Delta H^{\circ\ddagger}$ and a lower $\Delta S^{\circ\ddagger}$ for $\mathbf{p}-90°$ (Table 2). The extracted τ_{rot} values for $\mathbf{p}-90°$ and $\mathbf{t}80°$ are 0.5 μs and 21 ns, respectively (Table 2), which is well above τ_2 (6.16 ns) and τ_1 (2.45 ns) and well below τ_N (350 ms) and τ_U (1.5 ms). These lifetimes clearly reflect the population analysis result of parallel tempering, thus corroborating the use of Eyring plots over an extended temperature range. As expected for a solvent-exposed residue, $\Delta G^{\circ\ddagger}$ is highly correlated with SASA values, especially when the SASA standard deviation is taken into account (Table 2).

In principle, Eyring plots can also be constructed to obtain the individual rotamer transition rates at room temperature. From these rates, rotamer populations and reaction paths can be calculated. As shown in Fig. 4, straight curves were obtained for the total transition rates. For the individual transitions, however, prohibitively long simulation times would be required to obtain straight lines. Therefore, we will only report individual rates and reaction paths at a fixed temperature of 500 K.

Fig. 5 depicts all observed transitions and rate constants at 500 K on a $\chi1 \times \chi2$ map (see also Fig. 1 *d*). It is clear from the graph that $\chi1$ transitions are energetically more favorable than $\chi2$ transitions. This trend is even more pronounced as the temperature decreases. Note also the facile $\mathbf{m}-60° \leftrightarrow \mathbf{t}80°$ transition, which is a combination of $\chi1$ and $\chi2$ transition, and the absent $\mathbf{m}-60° \leftrightarrow \mathbf{m}120°$ transition. For $\mathbf{m}-60°$, a $\chi2$ transition via 0° with $\chi1$ fixed would lead to a steric clash between the Trp^{8} pyrrole ring and the backbone of Lys^{7}. When, nevertheless, $\chi2$ is forced to rotate, it must therefore be accompanied by a $\chi1$ rotation, leading to $\mathbf{t}80°$. Furthermore, the minimum-energy $\chi2$ angle for $\mathbf{m}-60°$ at

TABLE 2 Trp[8] rotamer thermodynamic and kinetic properties in 1HZB

	p−90°	t80°	p80°
Population*	0.71 ± 0.04	0.27 ± 0.03	0.016 ± 0.007
τ_{rot} (ns)†	(52 ± 13) × 10[1]	21 ± 2	0.93 ± 0.17
$\Delta H^{\circ\ddagger}$ (kJ mol^{-1})†	42.4 ± 1.7	20.4 ± 0.8	17.1 ± 1.3
$-T\Delta S^{\circ\ddagger}$ (kJ mol^{-1})†	−5.0 ± 1.1	9.0 ± 0.5	4.5 ± 0.8
$\Delta G^{\circ\ddagger}$ (kJ mol^{-1})†	37 ± 2	29.4 ± 0.9	21.6 ± 1.5
SASA (%)*	42.0 ± 0.3	44.4 ± 0.6	55.4 ± 1.2
SASA SD (%)*	3.8	5.6	3.7

τ_{rot}, rotamer lifetime at 300 K; $\Delta H^{\circ\ddagger}$, activation enthalpy; $\Delta S^{\circ\ddagger}$, activation entropy; $\Delta G^{\circ\ddagger}$, activation free energy; SASA, Trp[8] solvent-accessible surface area, relative to the tripeptide Ala-Trp-Ala; SD, standard deviation.
*Calculated as ensemble averages from the PT simulation.
†Calculated from the high-temperature simulations using transition state theory.

300 K is ≈30° larger than the ideal angle of −90° because of steric interactions with the Lys[7] side chain (Fig. 6). This $\chi 2$ equilibrium shift, accompanied by collisions with the very flexible Lys[7] side chain might help crossing the $\chi 2$ rotational barrier.

To quantify the mechanism, we computed the transition path at 500 K between the most stable rotamers **p**−90° and **t**80°. Both the forward and backward transitions follow the same path via **t**−110° (Fig. 5), in accordance with the principle of microscopic reversibility. The same pathway is followed at lower temperatures. At 525 K, however, **p**80° is found as the dominant intermediate state. This suggests that the pathway via **p**80° is entropically favored, whereas the **t**−110° route has a lower $\Delta H^{\circ\ddagger}$.

CONCLUSIONS

The parallel tempering method, combined with volume exchanges and native-state confinement allowed us to obtain precise rotamer distributions. In addition, a detailed study of local protein dynamics in the native state is made possible. In *Bc*-Csp 1HZB, two Trp rotameric states occupy a considerable amount of simulation time. This is confirmed by x-ray analysis and is in line with the dead-end elimination analysis. The rotamer distribution corresponds remarkably well with amplitude fractions of two fluorescence lifetimes. Solvent accessibilities correlate with acrylamide fluorescence quenching constants. A kinetic analysis reveals that the thermodynamically most stable rotamers are also the most kinetically stable ones. Both rotamers have sufficient kinetic stability to qualify as candidates for the origin of the biexponential fluorescence decay. The data further reveal that the Trp motions are strongly controlled by solvent exposure. In future work, we hope to apply these techniques to address challenging problems such as to what extent rotamer distributions are ubiquitous for exposed Trp residues and what rotation mechanisms are feasible for buried side chains.

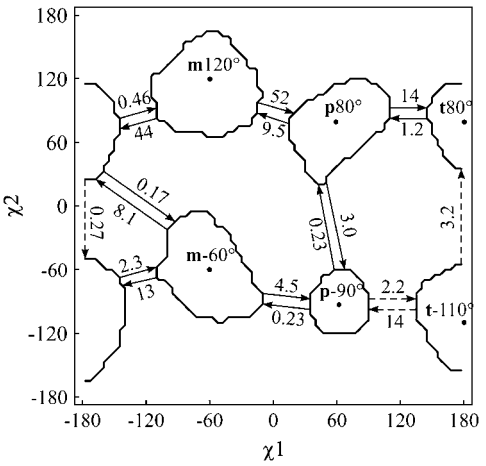

FIGURE 5 $\chi 1 \times \chi 2$ map of the six stable rotamers and a schematic representation of the observed transitions at 500 K, with transition rates given in ns^{-1}. The dashed arrows indicate the reaction path between **p**−90° and **t**80°. The contour lines enclose 95% of the population of each rotamer.

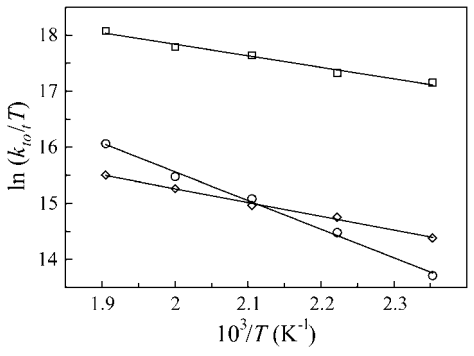

FIGURE 4 Eyring plots from the high-temperature dynamics for the three most stable rotamers, based on the total transition rate constants $k_{tot,i}$ (T). **p**−90° (○), **t**80° (◇), and **p**80° (□).

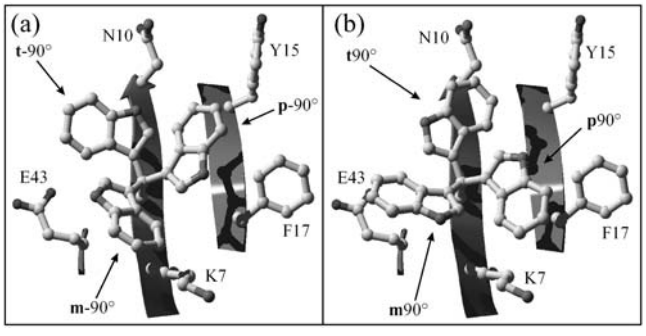

FIGURE 6 Tryptophan rotamers in *Bc*-Csp 1HZB. Superposition of the six Trp[8] rotamers in their ideal positions and the surface-exposed residues within a 5-Å radius of Trp[8]. (*a*) **m**−90°, **p**−90°, and **t**−90°. (*b*) **m**90°, **p**90°, and **t**90°.

We thank Prof. Dr. F. X. Schmid and Christine Magg (University of Bayreuth, Germany) for donating the *Bc*-Csp protein.

Financial support from Fonds voor Wetenschappelijk Onderzoek - Vlaanderen is gratefully acknowledged. M.H. was paid by the Interuniversitaire attractiepolen Phase V program, contract P5/33.

REFERENCES

1. Osterberg, F., G. M. Morris, M. F. Sanner, A. J. Olson, and D. S. Goodsell. 2002. Automated docking to multiple target structures: incorporation of protein mobility and structural water heterogeneity in AutoDock. *Proteins*. 46:34–40.
2. Kimura, S. R., R. C. Brower, S. Vajda, and C. J. Camacho. 2001. Dynamical view of the positions of key side chains in protein-protein recognition. *Biophys. J.* 80:635–642.
3. Schildbach, J. F., A. W. Karzai, B. E. Raumann, and R. T. Sauer. 1999. Origins of DNA-binding specificity: role of protein contacts with the DNA backbone. *Proc. Natl. Acad. Sci. USA*. 96:811–817.
4. Stapley, B. J., and A. J. Doig. 1997. Free energies of amino acid side-chain rotamers in α-helices, β-sheets and α-helix N-caps. *J. Mol. Biol.* 272:456–464.
5. Lindorff-Larsen, K., P. Rogen, E. Paci, M. Vendruscolo, and C. M. Dobson. 2005. Protein folding and the organization of the protein topology universe. *Trends Biochem. Sci*. 30:13–19.
6. Martin, A., I. Kather, and F. X. Schmid. 2002. Origins of the high stability of an in vitro-selected cold-shock protein. *J. Mol. Biol*. 318: 1341–1349.
7. Vivian, J. T., and P. R. Callis. 2001. Mechanisms of tryptophan fluorescence shifts in proteins. *Biophys. J*. 80:2093–2109.
8. Callis, P. R., and T. Q. Liu. 2004. Quantitative prediction of fluorescence quantum yields for tryptophan in proteins. *J. Phys. Chem. B*. 108:4248–4259.
9. Somers, K. R. F., P. Kruger, S. Bucikiewicz, M. De Maeyer, Y. Engelborghs, and A. Ceulemans. 2004. Protein simulations: The absorption spectrum of barnase point mutants. *Protein Sci*. 13:1823–1831.
10. Lasagna, M., E. Gratton, D. M. Jameson, and J. E. Brunet. 1999. Apohorseradish peroxidase unfolding and refolding: intrinsic tryptophan fluorescence studies. *Biophys. J*. 76:443–450.
11. Chen, Y., and M. D. Barkley. 1998. Toward understanding tryptophan fluorescence in proteins. *Biochemistry*. 37:9976–9982.
12. Sillen, A., J. F. Diaz, and Y. Engelborghs. 2000. A step toward the prediction of the fluorescence lifetimes of tryptophan residues in proteins based on structural and spectral data. *Protein Sci*. 9:158–169.
13. Hellings, M., H. Engelborghs, H. Deckmyn, K. Vanhoorelbeke, M. E. Schiphorst, J. W. N. Akkerman, and M. De Maeyer. 2004. Experimental indication for the existence of multiple Trp rotamers in von Willebrand factor A3 domain. *Proteins*. 57:596–601.
14. Adams, P. D., Y. Chen, K. Ma, M. G. Zagorski, F. D. Sonnichsen, M. L. McLaughlin, and M. D. Barkley. 2002. Intramolecular quenching of tryptophan fluorescence by the peptide bond in cyclic hexapeptides. *J. Am. Chem. Soc*. 124:9278–9286.
15. Fidy, J., M. Laberge, B. Ullrich, L. Polgar, Z. Szeltner, J. Gallay, and M. Vincent. 2001. Tryptophan rotamers that report the conformational dynamics of proteins. *Pure Appl. Chem*. 73:415–419.
16. Liu, T. Q., P. R. Callis, B. H. Hesp, M. de Groot, W. J. Buma, and J. Broos. 2005. Ionization potentials of fluoroindoles and the origin of nonexponential tryptophan fluorescence decay in proteins. *J. Am. Chem. Soc*. 127:4104–4113.
17. Hellings, M., M. De Maeyer, S. Verheyden, Q. Hao, E. J. M. Van Damme, W. J. Peumans, and Y. Engelborghs. 2003. The dead-end elimination method, tryptophan rotamers, and fluorescence lifetimes. *Biophys. J*. 85:1894–1902.
18. Hudson, B. S. 1999. An ionization/recombination mechanism for complexity of the fluorescence of tryptophan in proteins. *Accounts Chem. Res*. 32:297–300.
19. Lakowicz, J. R. 2000. On spectral relaxation in proteins. *Photochem. Photobiol*. 72:421–437.
20. Bajzer, Z., and F. G. Prendergast. 1993. A model for multiexponential tryptophan fluorescence intensity decay in proteins. *Biophys. J*. 65: 2313–2323.
21. Delbruck, H., U. Mueller, D. Perl, F. X. Schmid, and U. Heinemann. 2001. Crystal structures of mutant forms of the *Bacillus caldolyticus* cold shock protein differing in thermal stability. *J. Mol. Biol*. 313:359–369.
22. Weber, M. H., and M. A. Marahiel. 2003. Bacterial cold shock responses. *Sci. Prog*. 86:9–75.
23. Magg, C., and F. X. Schmid. 2004. Rapid collapse precedes the fast two-state folding of the cold shock protein. *J. Mol. Biol*. 335:1309–1323.
24. Garofoli, S., M. Falconi, and A. Desideri. 2004. Thermophilicity of wild type and mutant cold shock proteins by molecular dynamics simulation. *J. Biomol. Struct. Dyn*. 21:771–779.
25. Perl, D., and F. X. Schmid. 2001. Electrostatic stabilization of a thermophilic cold shock protein. *J. Mol. Biol*. 313:343–357.
26. Morra, G., M. Hodoscek, and E. W. Knapp. 2003. Unfolding of the cold shock protein studied with biased molecular dynamics. *Proteins*. 53:597–606.
27. Sugita, Y., and Y. Okamoto. 1999. Replica-exchange molecular dynamics method for protein folding. *Chem. Phys. Lett*. 314:141–151.
28. Frenkel, D., and B. Smit. 2002. Understanding Molecular Simulation. From Algorithms to Applications. Academic Press, London.
29. Garcia, A. E., and J. N. Onuchic. 2003. Folding a protein in a computer: an atomic description of the folding/unfolding of protein A. *Proc. Natl. Acad. Sci. USA*. 100:13898–13903.
30. Mueller, U., D. Perl, F. X. Schmid, and U. Heinemann. 2000. Thermal stability and atomic-resolution crystal structure of the *Bacillus caldolyticus* cold shock protein. *J. Mol. Biol*. 297:975–988.
31. Bevington, P. R. 1969. Gradient-expansion algorithm. *In* Data Reduction and Error Analyses for the Physical Sciences. McGraw-Hill, New York. 235–240.
32. Beechem, J. M., J. R. Knutson, J. B. A. Ross, B. W. Turner, and L. Brand. 1983. Global resolution of heterogeneous decay by phase modulation fluorometry: mixtures and proteins. *Biochemistry*. 22: 6054–6058.
33. More, J. J., and D. C. Sorensen. 1983. Computing a trust region step. *SIAM J. Sci. Stat. Comput*. 4:553–572.
34. Lakowicz, J. R. 1999. Principles of Fluorescence Spectroscopy. Kluwer Academic, New York. 238–264.
35. De Maeyer, M., J. Desmet, and I. Lasters. 2000. The dead-end elimination theorem: mathematical aspects, implementation, optimizations, evaluation, and performance. *Methods Mol. Biol*. 143: 265–304.
36. De Maeyer, M., J. Desmet, and I. Lasters. 1997. All in one: a highly detailed rotamer library improves both accuracy and speed in the modelling of sidechains by dead-end elimination. *Fold. Des*. 2:53–66.
37. Delhaise, P., M. Bardiaux, M. De Maeyer, M. Prevost, D. Vanbelle, J. Donneux, I. Lasters, E. Vancustem, P. Alard, and S. J. Wodak. 1988. The Brugel package: toward computer-aided design of macromolecules. *J. Mol. Graph*. 6:219.
38. Brooks, B. R., R. E. Bruccoleri, B. D. Olafson, D. J. States, S. Swaminathan, and M. Karplus. 1983. Charmm: a program for macromolecular energy, minimization, and dynamics calculations. *J. Comput. Chem*. 4:187–217.
39. Duan, Y., C. Wu, S. Chowdhury, M. C. Lee, G. M. Xiong, W. Zhang, R. Yang, P. Cieplak, R. Luo, T. Lee, J. Caldwell, J. M. Wang, and P. Kollman. 2003. A point-charge force field for molecular mechanics simulations of proteins based on condensed-phase quantum mechanical calculations. *J. Comput. Chem*. 24:1999–2012.
40. Case, D. A., T. A. Darden, T. E. Cheatham III, C. L. Simmerling, J. Wang, R. E. Duke, R. Luo, K. M. Merz, B. Wang, D. A. Pearlman, M. Crowley, S. Brozell, V. Tsui, H. Gohlke, J. Mongan, V. Hornak,

G. Cui, P. Beroza, C. Schafmeister, J. W. Caldwell, W. S. Ross, and P. A. Kollman. 2004. AMBER 8. University of California, San Francisco, CA.

41. Essmann, U., L. Perera, M. L. Berkowitz, T. Darden, H. Lee, and L. G. Pedersen. 1995. A smooth particle mesh Ewald method. *J. Chem. Phys.* 103:8577–8593.
42. Ryckaert, J.-P., G. Ciccotti, and H. J. C. Berendsen. 1977. Numerical integration of the Cartesian equations of motion of a system with constraints: molecular dynamics of *n*-alkanes. *J. Comput. Phys.* 23: 327–341.
43. Berendsen, H. J. C., J. P. M. Postma, W. F. Vangunsteren, A. Dinola, and J. R. Haak. 1984. Molecular-dynamics with coupling to an external bath. *J. Chem. Phys.* 81:3684–3690.
44. Jorgensen, W. L., J. Chandrasekhar, J. D. Madura, R. W. Impey, and M. L. Klein. 1983. Comparison of simple potential functions for simulating liquid water. *J. Chem. Phys.* 79:926–935.
45. Hubbard, S. J., and J. M. Thornton. 1993. NACCESS, Computer Program. Department of Biochemistry and Molecular Biology, University College, London.
46. Lee, B., and F. M. Richards. 1971. The interpretation of protein structures: estimation of static accessibility. *J. Mol. Biol.* 55:379–400.
47. Carter, P., C. A. F. Andersen, and B. Rost. 2003. DSSPcont: continuous secondary structure assignments for proteins. *Nucleic Acids Res.* 31:3293–3295.
48. Kabsch, W., and C. Sander. 1983. Dictionary of protein secondary structure: pattern-recognition of hydrogen-bonded and geometrical features. *Biopolymers.* 22:2577–2637.
49. Paschek, D., and A. E. Garcia. 2004. Reversible temperature and pressure denaturation of a protein fragment: a replica exchange molecular dynamics simulation study. *Phys. Rev. Lett.* 93:238105.
50. Allen, M. P., and D. J. Tildesley. 1987. Computer Simulation of Liquids. Oxford University Press, New York.
51. Zuniga, I., I. Bahar, R. Dodge, and W. L. Mattice. 1991. Molecular-dynamics analysis of transitions between rotational isomers in polymethylene. *J. Chem. Phys.* 95:5348–5354.
52. Park, S., M. K. Sener, D. Y. Lu, and K. Schulten. 2003. Reaction paths based on mean first-passage times. *J. Chem. Phys.* 119:1313–1319.
53. Lovell, S. C., J. M. Word, J. S. Richardson, and D. C. Richardson. 2000. The penultimate rotamer library. *Proteins.* 40:389–408.
54. Perl, D., G. Holtermann, and F. X. Schmid. 2001. Role of the chain termini for the folding transition state of the cold shock protein. *Biochemistry.* 40:15501–15511.
55. Schueler-Furman, O., C. Wang, P. Bradley, K. Misura, and D. Baker. 2005. Progress on modeling of protein structures and interactions. *Science.* 310:638–642.
56. Chung, S. Y., and S. Subbiah. 1996. How similar must a template protein be for homology modeling by side-chain packing methods? Biocomputing: Proc. 1996 Pacific Symposium. Lawrence Hunter and Teri Klein, editors. World Scientific Publishing, Singapore. 126–141.
57. Eyal, E., S. Gerzon, V. Potapov, M. Edelman, and V. Sobolev. 2005. The limit of accuracy of protein modeling: influence of crystal packing on protein structure. *J. Mol. Biol.* 351:431–442.
58. Zhang, X. J., J. A. Wozniak, and B. W. Matthews. 1995. Protein flexibility and adaptability seen in 25 crystal forms of T4 lysozyme. *J. Mol. Biol.* 250:527–552.
59. Zeeb, M., M. H. Jacob, T. Schindler, and J. Balbach. 2003. N-15 relaxation study of the cold shock protein CspB at various solvent viscosities. *J. Biomol. NMR.* 27:221–234.
60. Perl, D., U. Mueller, U. Heinemann, and F. X. Schmid. 2000. Two exposed amino acid residues confer thermostability on a cold shock protein. *Nat. Struct. Biol.* 7:380–383.